Science Advances
AAAS

Supplementary Materials for

Eyedrop-based macromolecular ophthalmic drug delivery for ocular fundus disease treatment

Jingjing Shen *et al.*

Corresponding author: Zhuang Liu, zliu@suda.edu.cn; Qian Chen, chenqian@suda.edu.cn;
Ping Gu, guping2009@sjtu.edu.cn; Xiaofeng Zhang, zhangxiaofeng@suda.edu.cn

Sci. Adv. **9**, eabq3104 (2023)
DOI: 10.1126/sciadv.abq3104

The PDF file includes:

Figs. S1 to S32
Tables S1 and S2
Legend for movie S1

Other Supplementary Material for this manuscript includes the following:

Movie S1

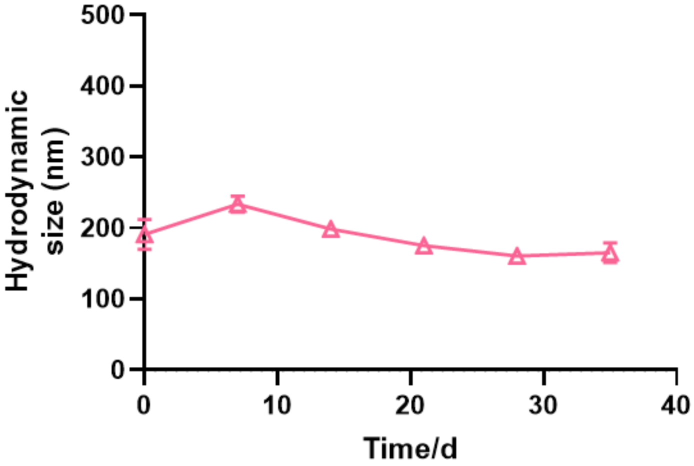

fig. S1. The size distribution of FCS/IgG for 1 to 5 weeks.

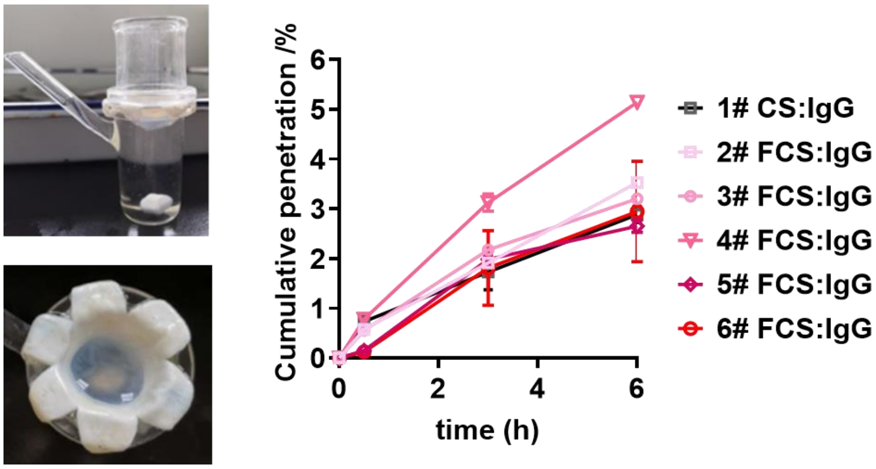

fig. S2. Franz diffusion cell device modified with rabbit corneas and the cumulative penetration percentages of different groups.

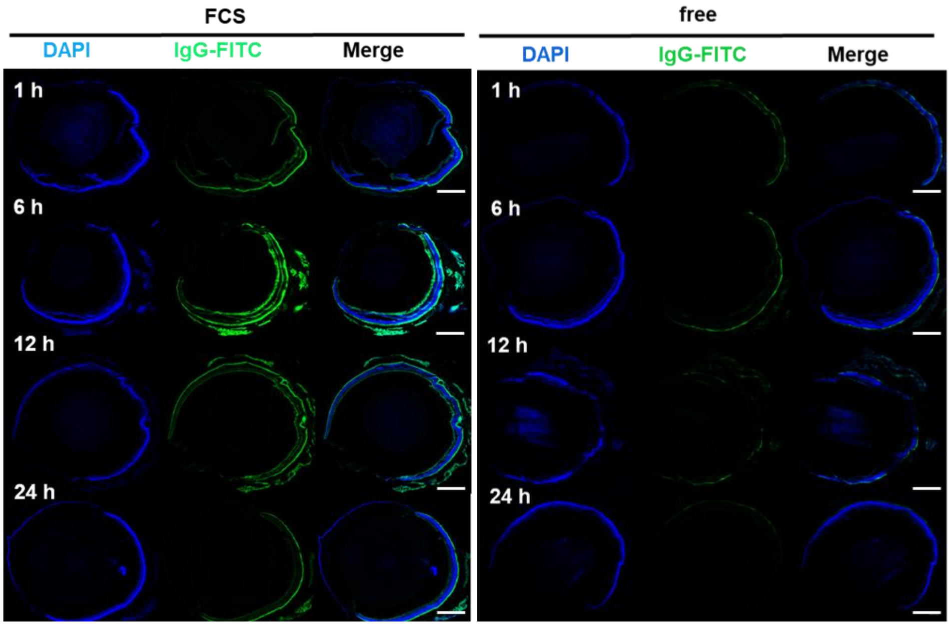

fig. S3. Confocal images of eyeballs collected from mice after treatment with FCS/IgG-FITC nanocomplexes or free IgG-FITC at 1, 6, 12, and 24 h time points (IgG-FITC: green, DAPI: blue, scale bars: 500 μm).

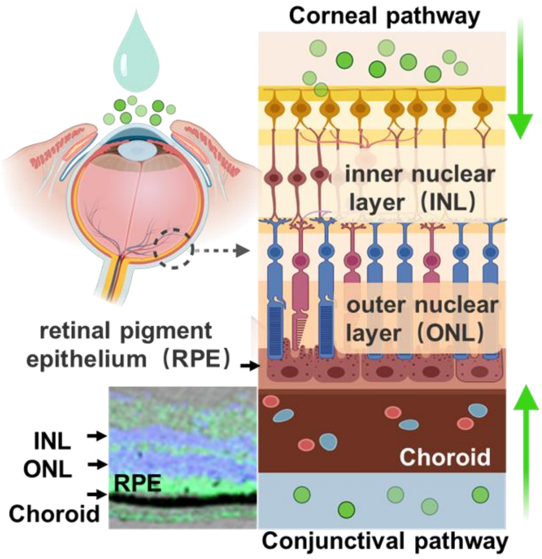

fig. S4. Schematic showing the structure of the retina and choroid.

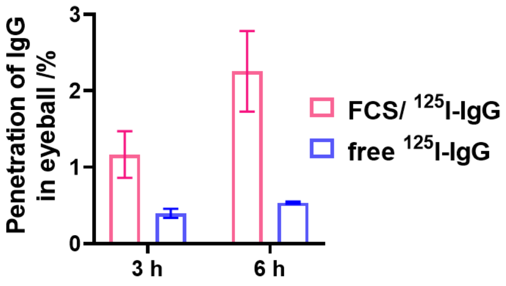

fig. S5. After labelling rat IgG with radioisotope ^{125}I, the FCS/^{125}I-IgG or free ^{125}I-IgG were dropped on mouse eyes (n=3). After three or six hours, the eyes were collected and their radioactivities were measured by a gamma counter, after removing residual ^{125}I on the ocular surface by PBS rinsing. FCS/^{125}I-IgG showed much higher radioactivity retention in mouse eyes at both time points.

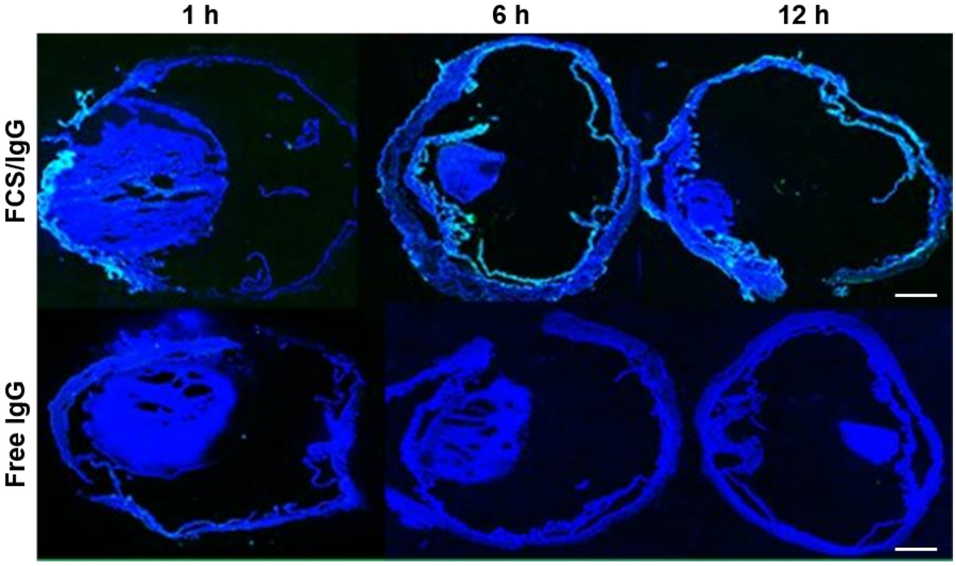

fig. S6. Confocal images of eyeballs collected from rabbits after FCS/IgG-FITC nanocomplex or free IgG-FITC eyedrop treatment at different time points (IgG-FITC: green, DAPI: blue, scale bars: 5 mm).

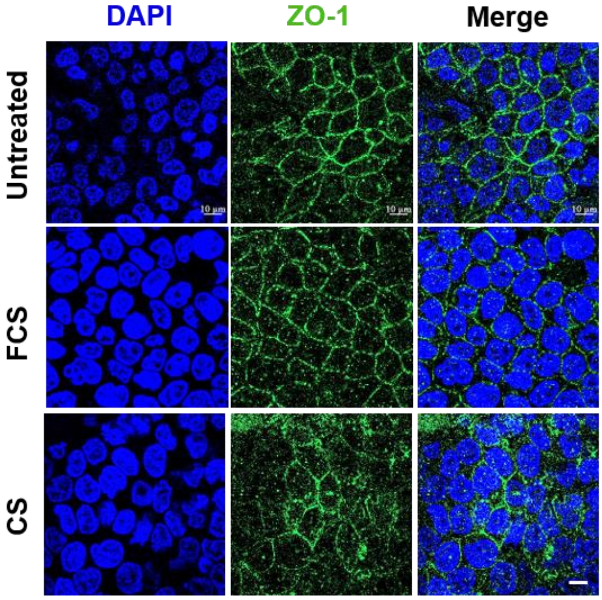

fig. S7. Confocal images indicating the distribution of ZO-1 on HCECs monolayer after incubation with the FCS/IgG nanocomplex (scar bar: 10 μm).

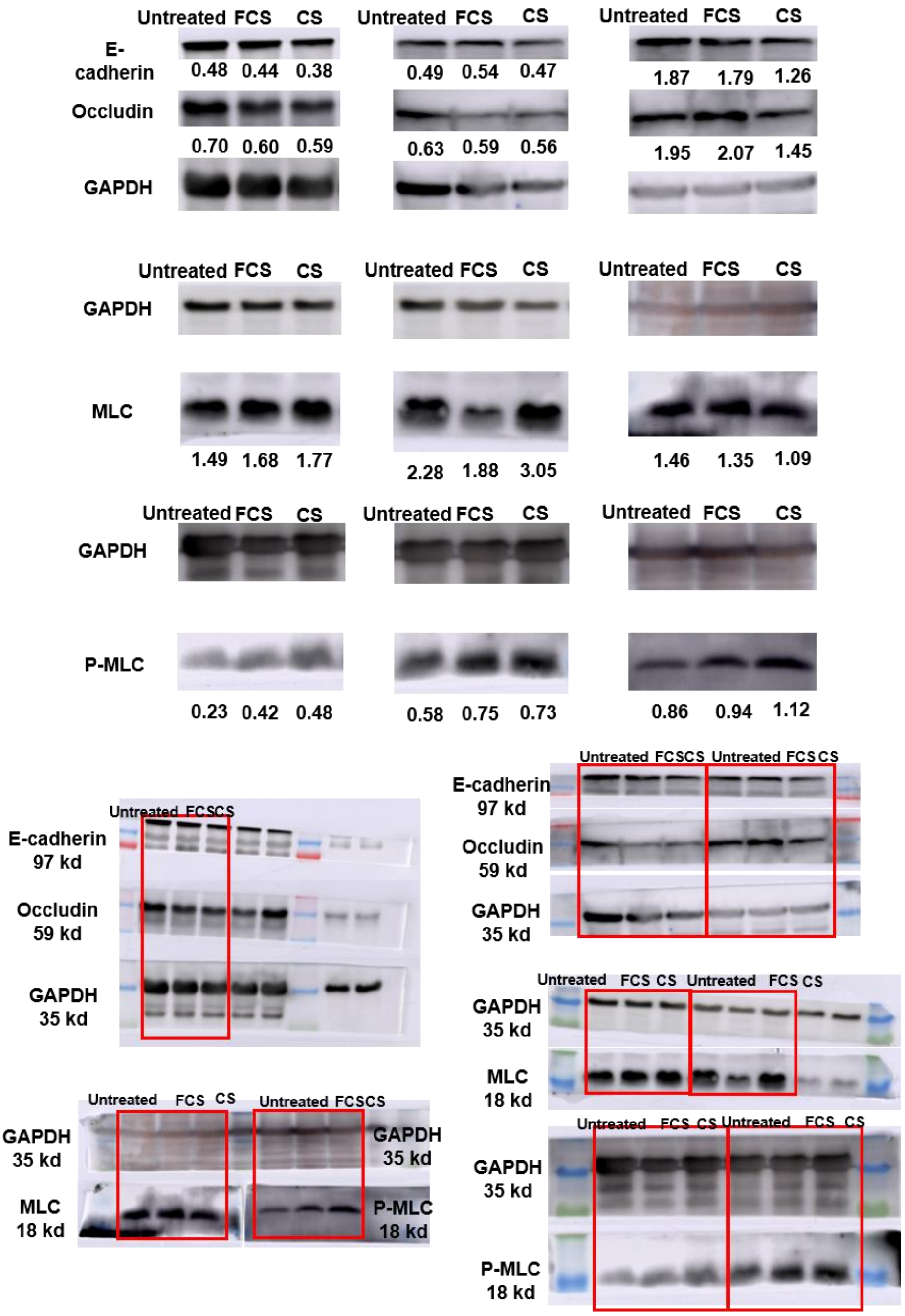

fig. S8. Western blotting images showing the expression of occludin, e-cadherin, MLC, and p-MLC and the original images of western blotting.

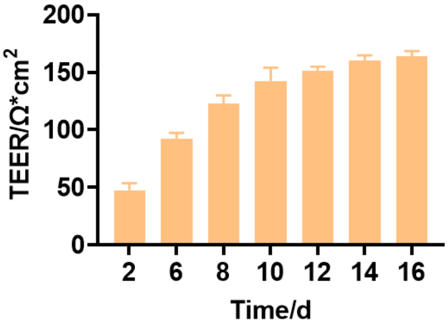

Fig. S9. Formation of HCECs monolayer detected by TEER.

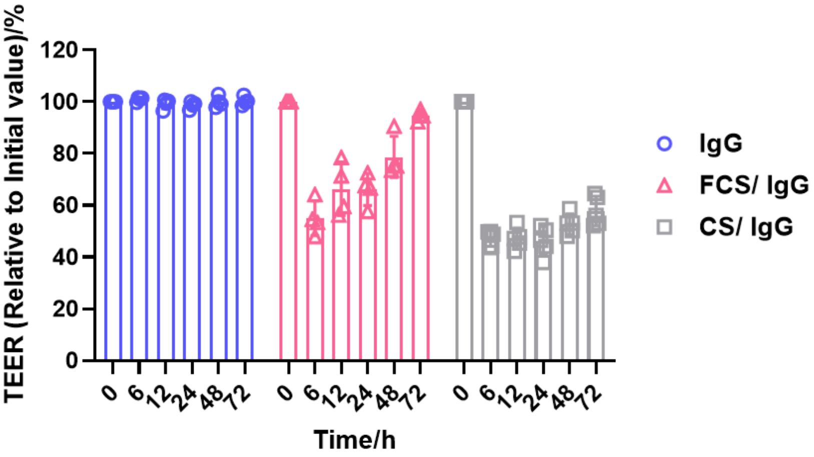

fig. S10. TEER of HCECs after different treatments for 6 hours.

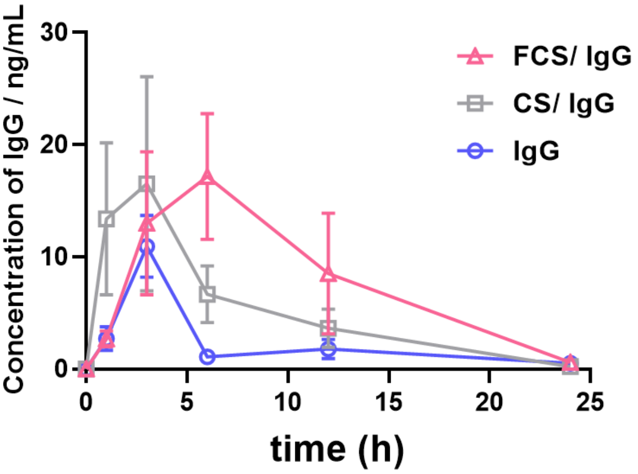

fig. S11. The IgG concentration in blood after different treatments for 0, 1, 3, 6, 12, 24 hours.

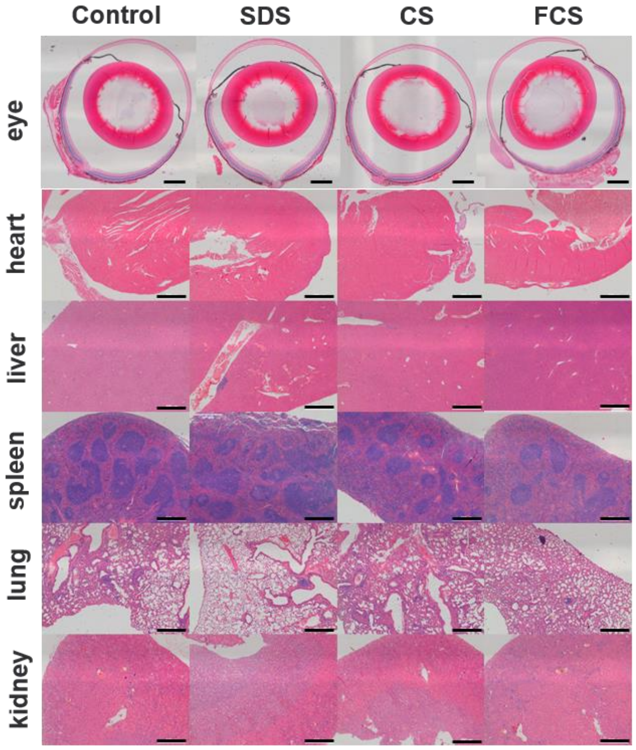

fig. S12. H&E staining slices of different organs including eye, heart, liver, bladder, spleen and lung collected from mice in different groups (scale bars: 200 μm).

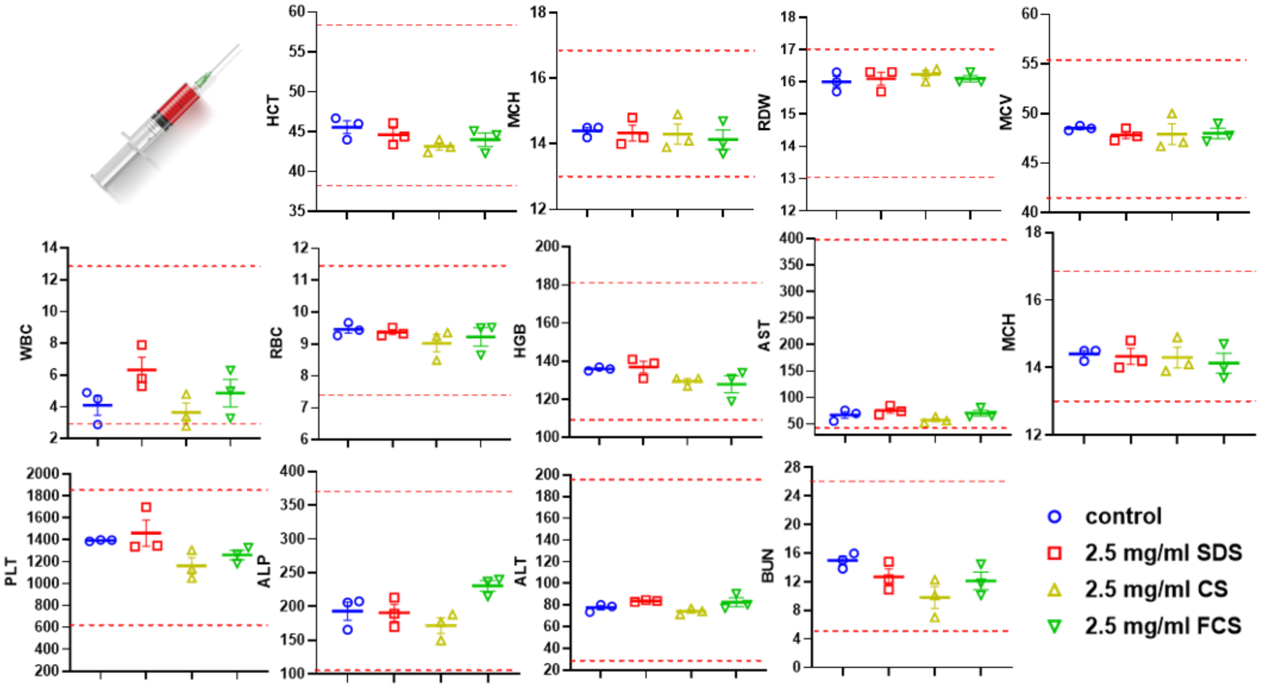

fig. S13. Blood biochemistry and complete blood analysis of mice receiving different treatments. The following parameters were tested: alanine aminotransferase (ALT); aspartate aminotransferase (AST); alkaline phosphatase (ALP); blood urea nitrogen (BUN); white blood cell (WBC) counts; red blood cell (RBC) counts; haemoglobin

(HGB); haematocrit value (HCT); mean corpuscular volume (MCV); red cell volume distribution width (RDW); mean corpuscular haemoglobin (MCH); mean corpuscular haemoglobin (MCH) and platelets (PLT).

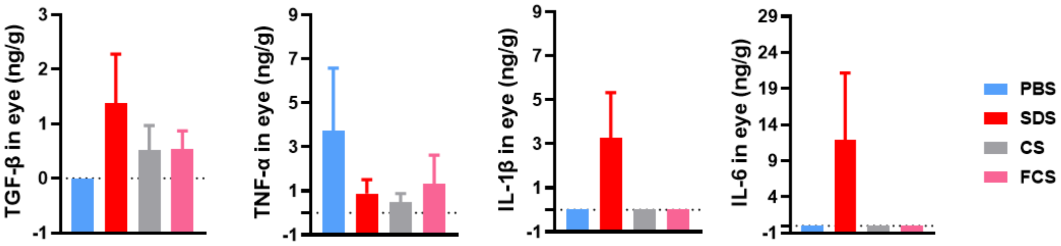

fig. S14. Concentrations of inflammatory cytokines, including TGF-β, TNF-α, IL-1β and IL-6, in the eyeball of mice after different treatments.

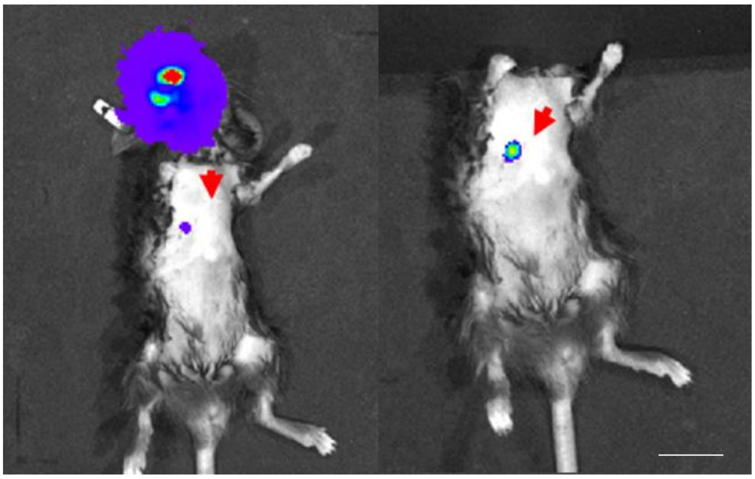

fig. S15. Representative in vivo bioluminescence images of mice with choroidal melanoma metastases without treatment (scale bars: 1 cm).

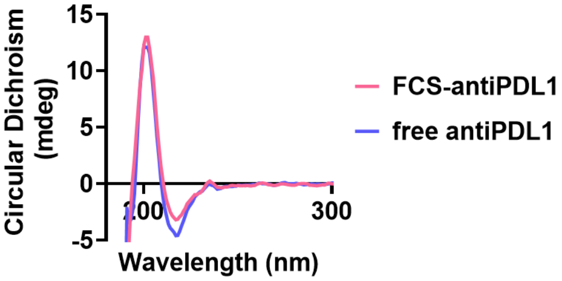

fig. S16. Circular dichroism spectrum of FCS/anti-PDL1 and free anti-PDL1.

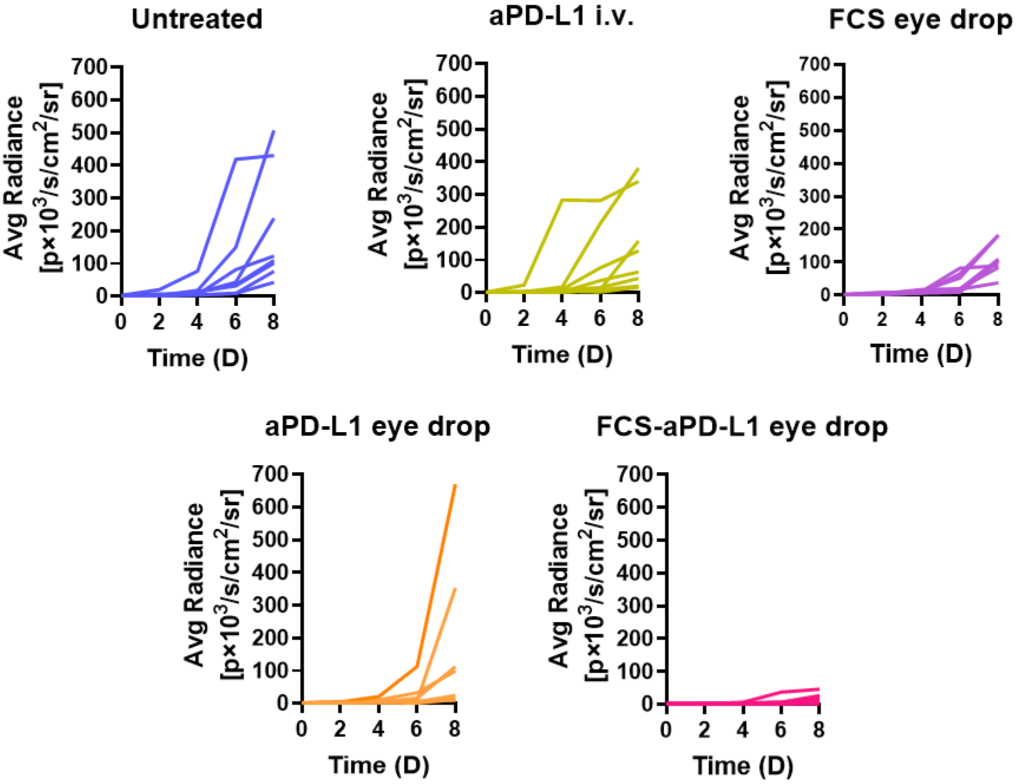

fig. S17. Individual bioluminescence signal intensity of choroidal melanoma after different treatments (n=8).

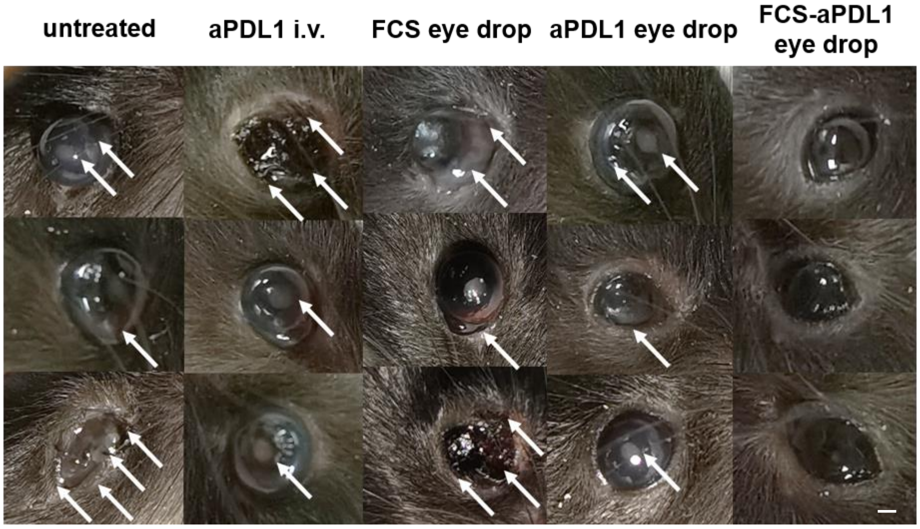

fig. S18. Representative photographs of choroidal melanoma-bearing eyes after different treatments on day 10. The arrows represented the choroidal melanoma (scale bars: 1 mm).

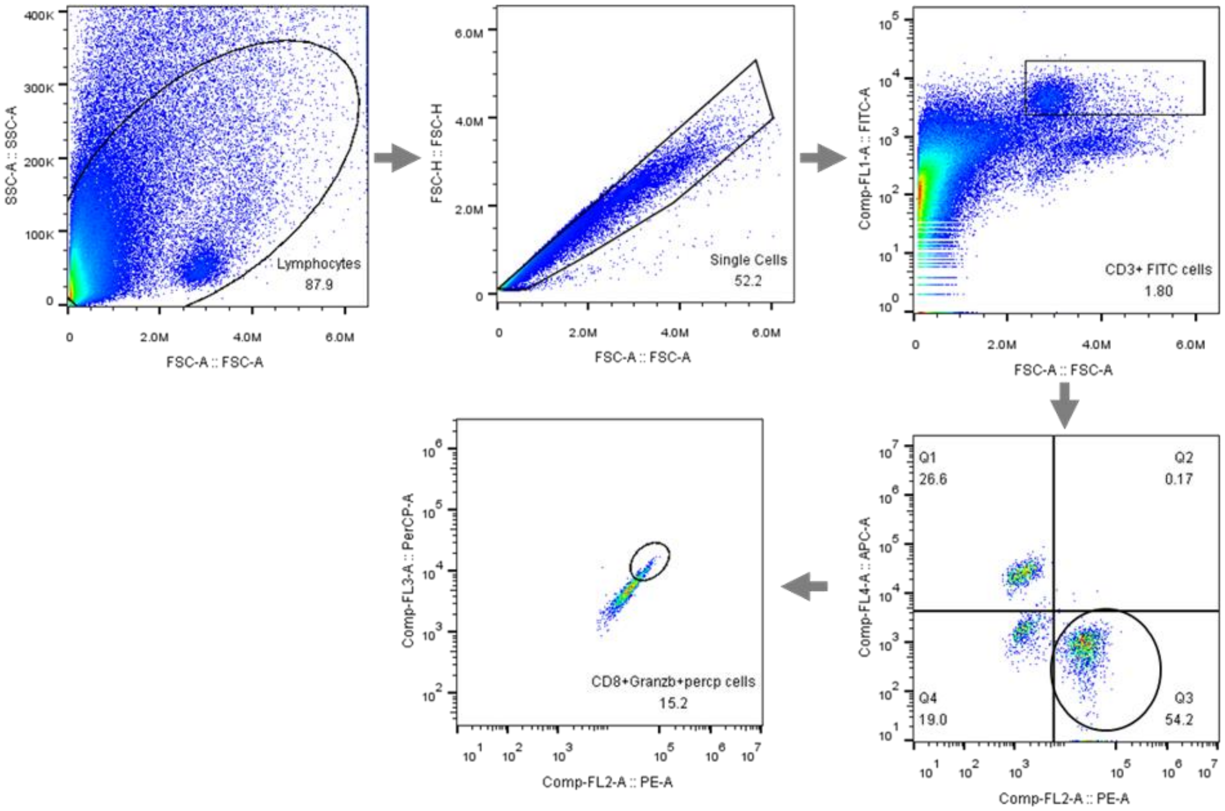

fig. S19. Gating strategy of CD8+ T cells and CD4+ T cells in choroidal melanoma.

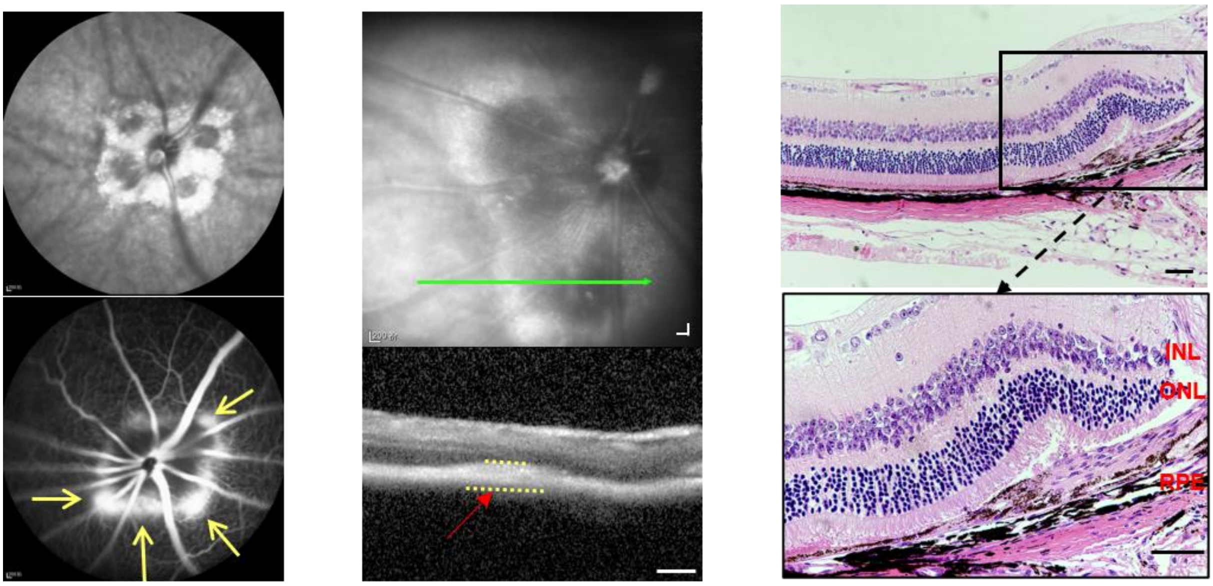

fig. S20. Representative OCT images, FFA images and H&E staining images of laser-induced CNV in mice (INL=inner nuclear layer, ONL=outer nuclear layer, RPE=retinal pigmented epithelial layer). The arrows and dotted lines point to the CNV position (OCT image scale bars: 200 μm; H&E image scale bars: 100 μm).

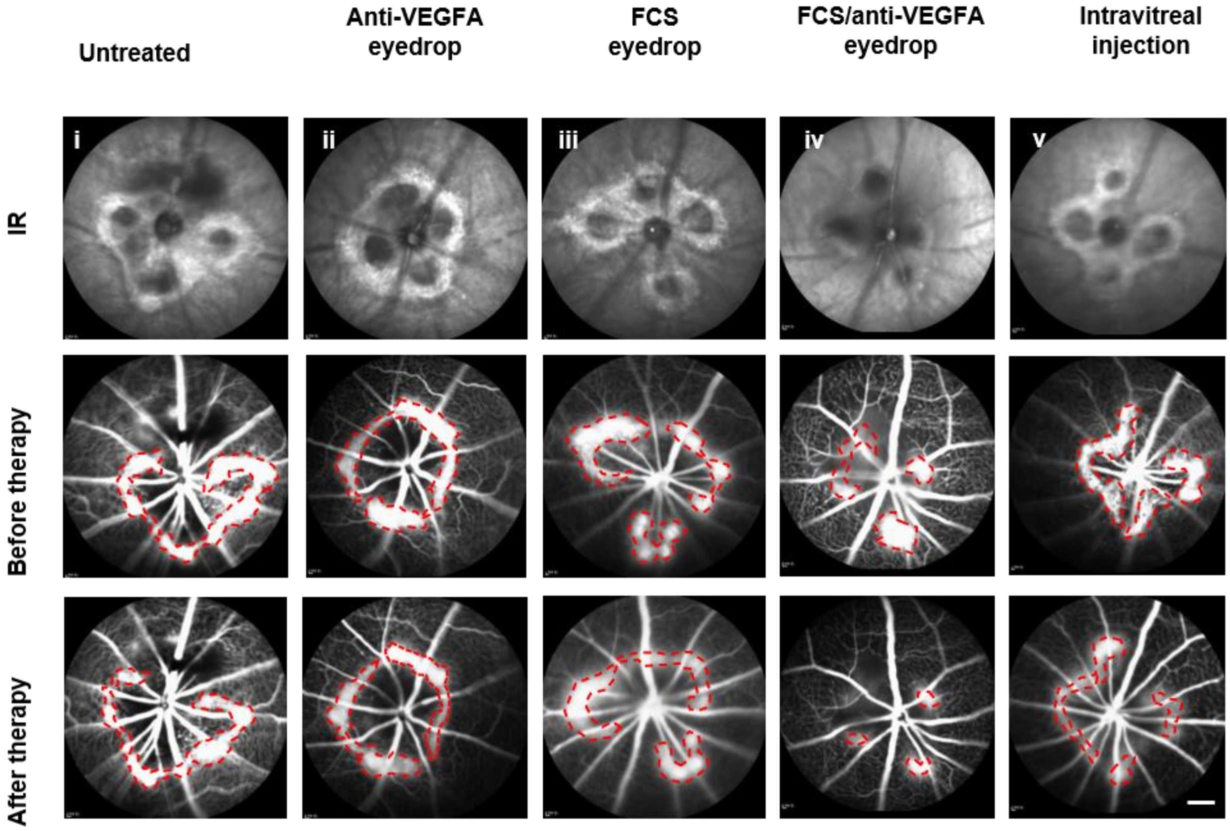

fig. S21. Representative FFA images of individual lesions in CNV-bearing mice before and after different treatments. The dotted portion pointed to CNV positions (scale bars: 10 µm).

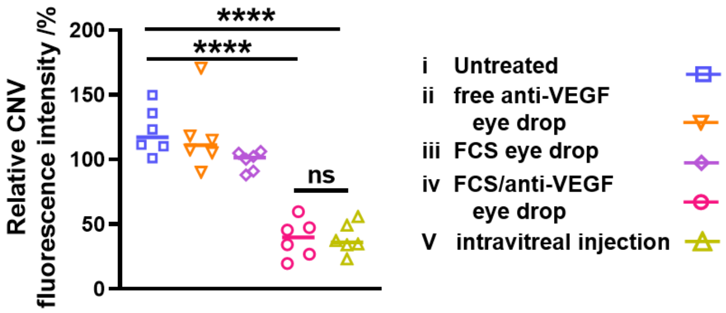

fig. S22. Statistical analysis of the relative fluorescence intensity of fluorescein sodium in the leakage of angiogenic vessels in CNV mice by J imaging. Data were represented as means ± SD. P values were calculated by using one-way ANOVA ($^{*}P < 0.05$, $^{**}P < 0.01$, $^{***}P < 0.001$, and $^{****}P < 0.0001$).

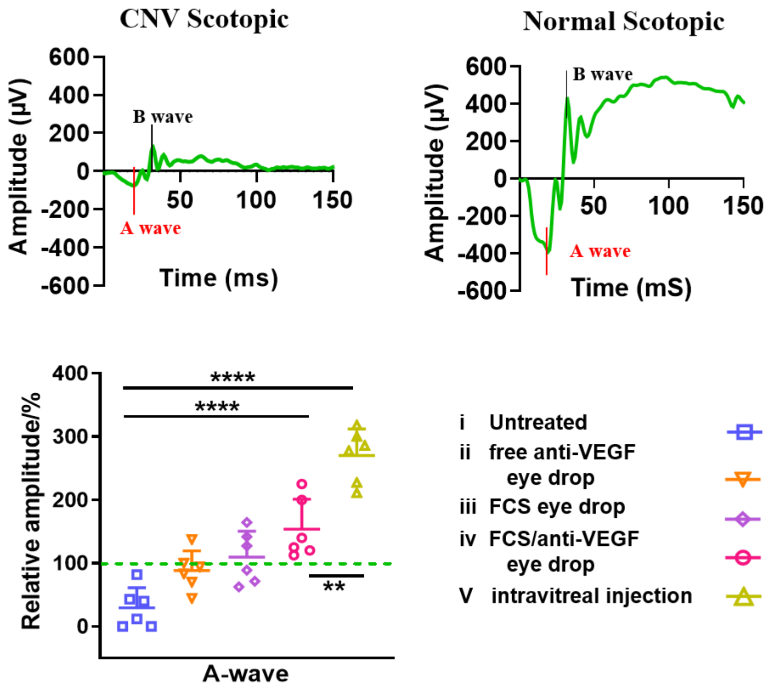

fig. S23. Representative ERG wave responses of normal mice and laser-induced CNV mice in scotopic conditions as well as statistical analysis of the A wave measured by ERG of mice after different treatments. Data were represented as means ± SD. P values were calculated by using one-way ANOVA ($^{*}P < 0.05$, $^{**}P < 0.01$, $^{***}P < 0.001$, and $^{****}P < 0.0001$).

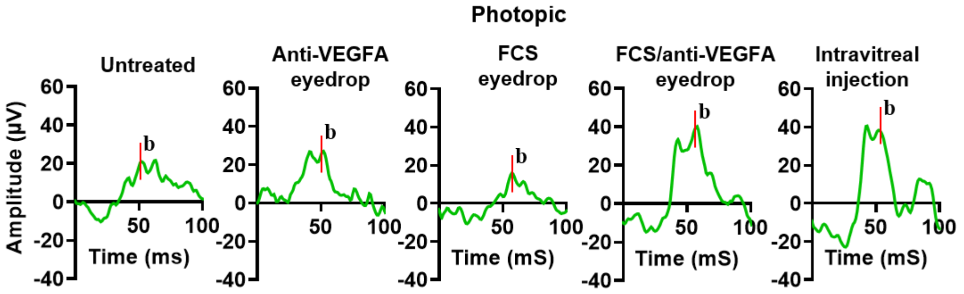

fig. S24. Representative ERG wave responses of CNV-bearing mice after different treatments in photopic conditions.

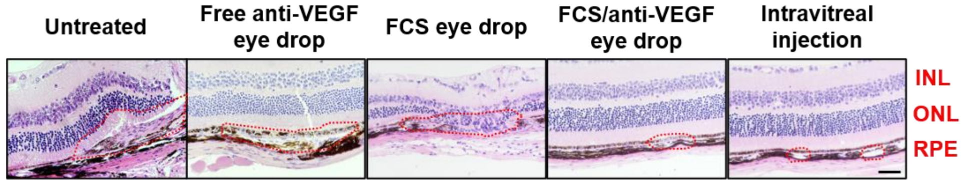

fig. S25. Representative H&E staining images of laser-induced CNV in the choroid and retina of mice after different treatments. The dotted lines point to the CNV position (scale bars: 100 μm).

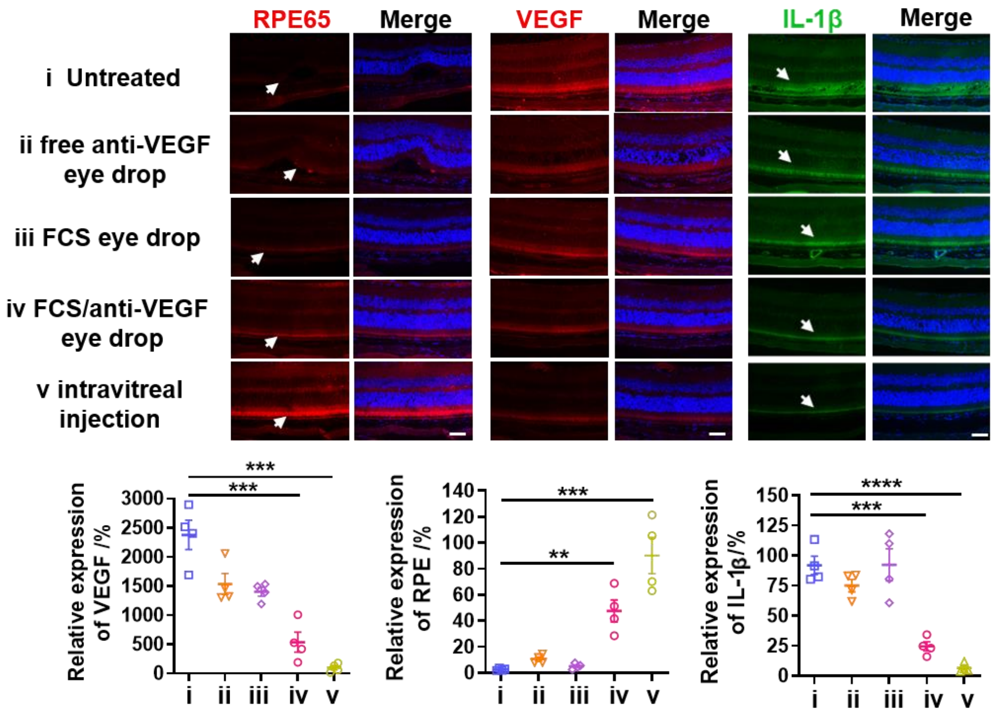

Fig. S26. Representative immunofluorescence staining images of RPE65, VEGF and IL-1β expressed in the retinas of CNV-bearing mice after different treatments (scale bars: 100 μm). The immunofluorescence staining images of RPE65, VEGF and IL-1β expressed in the retina of CNV-bearing mice analyzed by Image J.

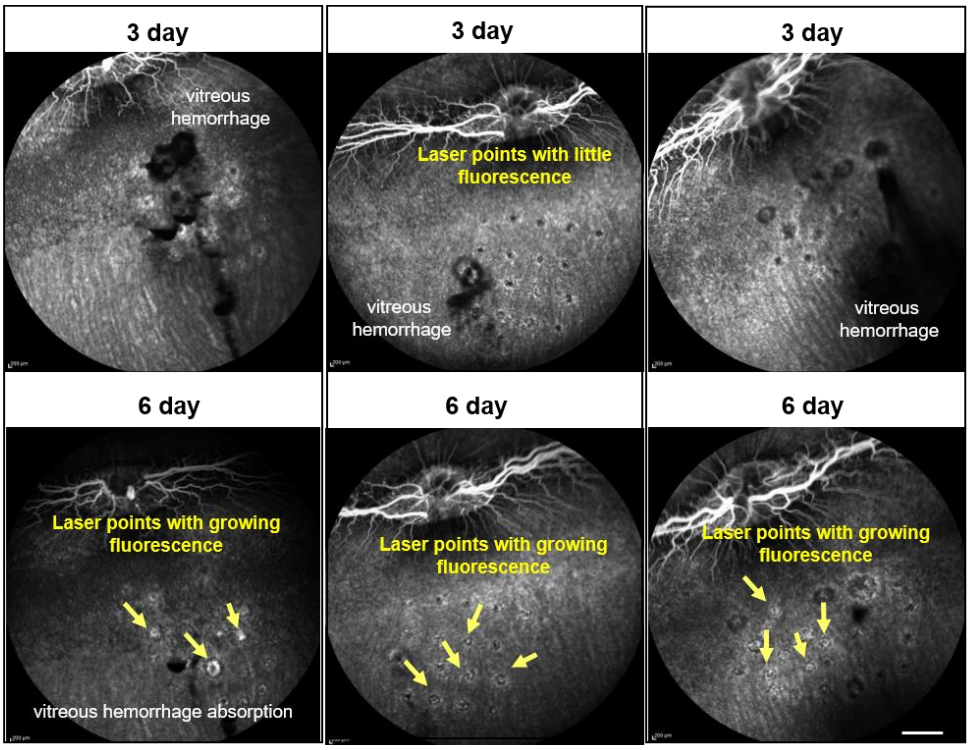

fig. S27. FFA images showing the position of laser spots and fluorescence leakage in the rabbit. Representative FFA images of laser-induced CNV in rabbits on days three and six. The arrows show enhanced fluorescence with time, and fluorescent leakage laser spots were observed on day six (scale bars: 2 mm).

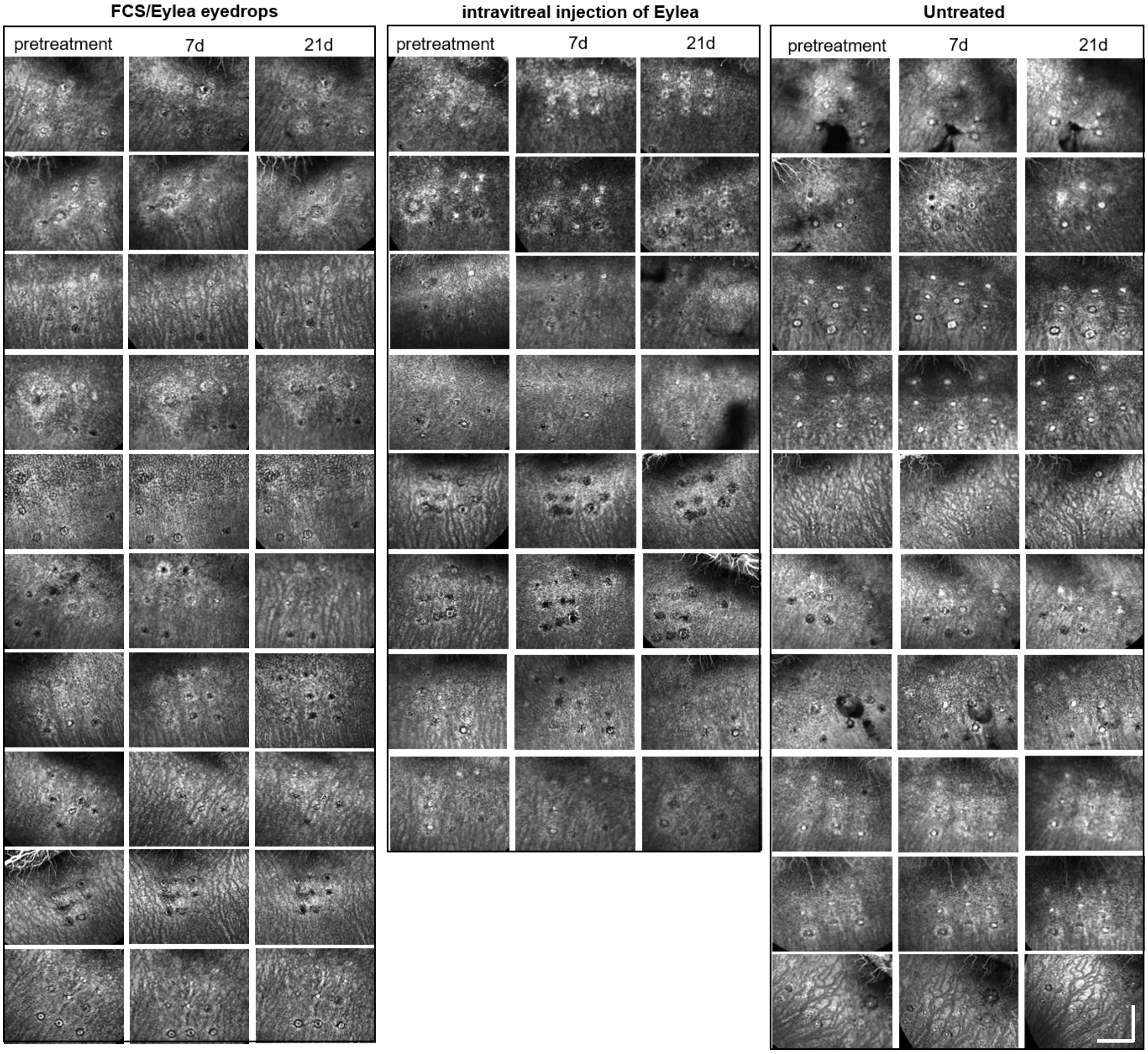

Fig. S28. Individual FFA images of lesions in CNV-bearing rabbits during treatment on days 0, 7 and 21 (FCS/Eylea nanocomplex eyedrops, n=10; intravitreal injection of Eylea, n=8; PBS eyedrops, n=10) (scale bars: 2 mm).

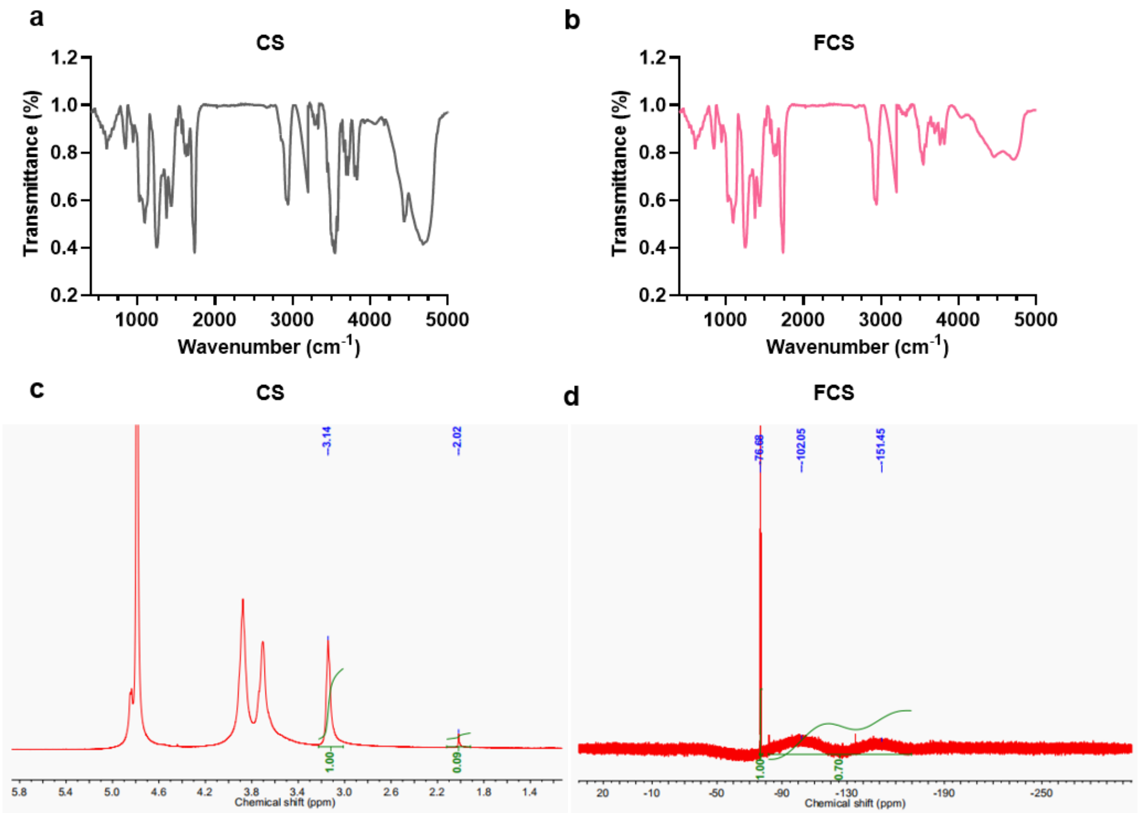

Fig, S29. The Fourier Transform infrared spectroscopy (FTIR) and NMR spectra of chitosan and fluorinated chitosan.

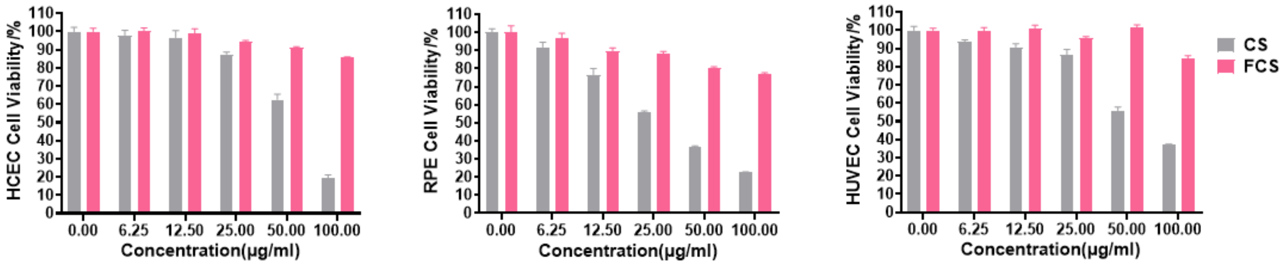

Fig. S30. Relative viabilities of HCEC cells, RPE cells, and HUVEC cells after incubated with different concentrations of FCS, CS, or PBS for 24 h.

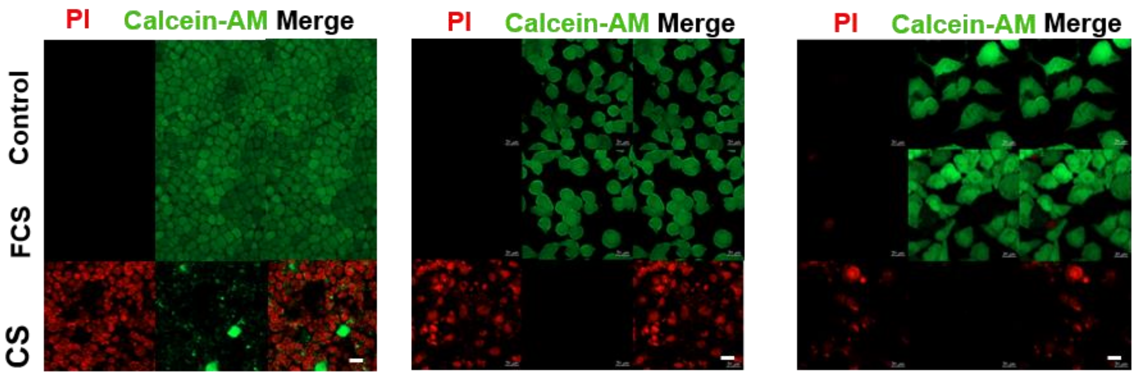

Fig. S31. Dead or alive staining of HCEC cells, RPE cells, and HUVEC cells after incubated with FCS, CS, or PBS for 24 h (red: dead cells, green: alive cells, scale bar: 10 μm).

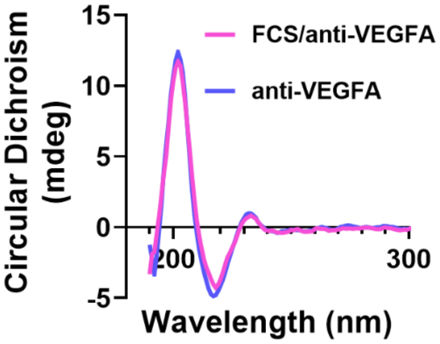

Fig. S32. Circular dichroism spectra of FCS/anti-VEGFA and anti-VEGFA.

Table S1. The FCS/IgG and CS/IgG in PBS with or without serum for three hours and detected the amount of free IgG after ultracentrifugation.

Drug loading /%	**FCS/IgG**	**CS/IgG**
In PBS (mean ± SD)	95.52 ± 0.83	81.12 ± 0.34
In FBS (mean ± SD)	70.56 ± 5.28	38.48 ± 7.01

Table S2. The particle sizes, surface charges, drug loading and drug encapsulation efficiencies of FCS (or CS)/IgG nanocomplexes.

Mean ± SD	**FCS/IgG**	**CS/IgG**
Hydrodynamic size /nm	180.10 ± 53.01	1159.67 ± 89.35
Zeta /mV	25.80 ± 1.10	32.00 ± 0.82
Drug loading /%	95.52 ± 0.83	81.12 ± 0.34
Drug encapsulation efficiency /%	46.19 ± 1.71	38.96 ± 0.68

Movie S1. Rabbit eye stimulation experiment